Properties of Jupiter's magnetospheric turbulence observed by the Galileo spacecraft

Chihiro Tao, Fouad Sahraoui, Dominique Fontaine, Judith De Patoul, Thomas Chust, Satoshi Kasahara, Alessandro Retinò

AGU PUBLICATIONS

JGR

Journal of Geophysical Research: Space Physics

RESEARCH ARTICLE
10.1002/2014JA020749

Key Points:
- Characterize Jupiter's magnetospheric turbulence and its spatial variations
- Spectral breaks are seen around heavy ion characteristic scales
- Intermittent cascade is associated with various spectral indices

Correspondence to:
C. Tao,
chihiro.tao@irap.omp.eu

Citation:
Tao, C., F. Sahraoui, D. Fontaine, J. de Patoul, T. Chust, S. Kasahara, and A. Retinò (2015), Properties of Jupiter's magnetospheric turbulence observed by the Galileo spacecraft, *J. Geophys. Res. Space Physics*, *120*, 2477–2493, doi:10.1002/2014JA020749.

Received 17 OCT 2014
Accepted 2 MAR 2015
Accepted article online 5 MAR 2015
Published online 1 APR 2015

Properties of Jupiter's magnetospheric turbulence observed by the Galileo spacecraft

Chihiro Tao[1,2], Fouad Sahraoui[2], Dominique Fontaine[2], Judith de Patoul[2,3], Thomas Chust[2], Satoshi Kasahara[4], and Alessandro Retinò[2]

[1]IRAP, Université de Toulouse/UPS-OMP/CNRS, Toulouse, France, [2]LPP, Ecole Polytechnique/CNRS, Palaiseau, France, [3]Aix Marseille Université, CNRS, LAM UMR 7326, Marseille, France, [4]ISAS/JAXA, Sagamihara, Japan

Abstract In collisionless plasmas, turbulence is thought to play an important role in mass transport and energy dissipation. Magnetic fluctuations in the Jovian magnetosphere are essential in a turbulent state. Previous studies of that turbulence have focused on the large scales using low time resolution of magnetic field data. Here we extend those studies to cover a wider range of scales by combining both low and high-time-resolution data of Galileo magnetometer. We use particle data from the plasma instrument and include energetic particle contributions to estimate the local plasma parameters. We obtain 11 power spectra of magnetic field in the frequency range of 10^{-4}–1 Hz, which covers both magnetohydrodynamics and ion kinetic scales. The frequencies of the evidenced spectral breaks are found to be relatively well correlated with the characteristic scales of heavy ion. The spectral indices below and above the spectral breaks are found to be broad and cover the ranges of 0.6–1.9 and 1.7–2.5, respectively. An analysis of higher-order statistics shows an intermittent feature of the turbulence, found to be more prominent in the plasma sheet than in the lobe. Furthermore, a statistical survey of the power of the fluctuations using low-time-resolution data suggests a radially varying dawn-dusk asymmetry: the total power is larger in the duskside (dawnside) at $<50\ R_J$ ($>80\ R_J$), which would reflect flow shear and global magnetospheric activity.

1. Introduction

Turbulence is ubiquitous in fluids and magnetized plasmas. In space and astrophysical plasmas, magnetic turbulence is believed to play a key role in different processes such as mass and energy transports, particle heating, or acceleration [e.g., *Bruno and Carbone*, 2005; *Schekochihin et al.*, 2009; *Zimbardo et al.*, 2010]. The near-Earth space, i.e., the Earth's magnetosphere and the solar wind at 1 AU, provides the best plasma laboratory to investigate such dynamical processes, in particular because of the availability of a huge amount of high-quality data provided by numerous space missions, from the earlier ones, e.g., Voyager, to the more recent ones such as Wind, Cluster, and Stereo. In the solar wind, general properties of the turbulence have been evidenced. The most studied one is the turbulence energy spectra, known to show distinct spectral breaks occurring near different characteristic scales (e.g., the ion and the electron characteristic scales). These breaks separate four zones of scales with different scaling laws on the observed frequency f: the energy-containing scales with a spectrum close to f^{-1} [*Bruno and Carbone*, 2005], the inertial range having the so-called Kolmogorov scaling $\sim f^{-5/3}$, the dispersive range (known also as the dissipation range) with scaling $\sim f^{-2.8}$ in the sub–ion scales [*Leamon et al.*, 1998; *Smith et al.*, 2006; *Sahraoui et al.*, 2009, 2010; *Alexandrova et al.*, 2012], and the sub–electron range with a scaling close to f^{-4} [*Sahraoui et al.*, 2009, 2010, 2013]. For sub–electron scales, other studies have reported exponential-like spectra [*Alexandrova et al.*, 2012]. Several scenarios have been proposed to explain the steepening of the spectra near the ion kinetic scale, such as the transition from Alfvén to kinetic Alfvén wave (KAW) turbulence [e.g., *Howes et al.*, 2008; *Sahraoui et al.*, 2010], the compressible Hall effects [e.g., *Alexandrova et al.*, 2008], and the energy dissipation by two-dimensional magnetic reconnection [*Matthaeus and Lamkin*, 1986]. The analyses of the solar wind plasma at different heliospheric distances, typically between 0.3 and 5 AU, by *Perri et al.* [2010] and *Bourouaine et al.* [2012] showed that spectral break frequency have small variations within the range of 0.2–0.4 Hz; a better correlation of the spectral breaks with the ion inertial scale was also found.

While there is a general consensus that turbulence in the inertial range is essentially dominated by shear Alfvénic fluctuations (a small compressible component representing about 10% in the total power exist though [see, e.g., *Klein et al.*, 2012]), the nature of the plasma modes carrying the turbulence cascade at

sub–ion scales remains very controversial. Two main candidates are debated: the KAW turbulence [*Howes et al.*, 2008; *Bale et al.*, 2005; *Sahraoui et al.*, 2009, 2010; *Podesta and TenBarge*, 2012; *Chen et al.*, 2013] and the whistler turbulence [e.g., *Stawicki et al.*, 2001; *Gary and Smith*, 2009].

In comparison with solar wind turbulence, turbulence in the magnetosphere is less known. In the magnetosheath, the most studied turbulent region of the magnetosphere, a few studies revealed similarities with solar wind turbulence: (i) a strong anisotropy ($k_{//} \ll k_{\perp}$) both at sub–proton and electron scales [*Sahraoui et al.*, 2004, 2006; *Mangeney et al.*, 2006] and (ii) the presence of kinetic instabilities and nonlinear structures [*Sahraoui et al.*, 2004; *Sahraoui*, 2008; *Alexandrova and Saur*, 2008]. Major differences exist though; e.g., (i) magnetosheath turbulence evolves in a "confined" space limited by the bow shock and the magnetopause; these boundaries may influence the anisotropy of the turbulence [*Sahraoui et al.*, 2006; *Yordanova et al.*, 2008]; (ii) the dominance of zero-frequency compressible fluctuations (e.g., mirror modes [*Sahraoui et al.*, 2006]); and (iii) the spectra at sub–electron scales were found steeper in the magnetosheath than in the solar wind [*Huang et al.*, 2014]. Magnetotail turbulence is also constrained by boundaries and is generally embedded within plasmoids and bursty bulk flows due to magnetotail reconnection events [e.g., *Hoshino et al.*, 1994; *Vörös et al.*, 2004a].

Observational studies have also targeted turbulence in other planetary environments, such as Jupiter [e.g., *Saur et al.*, 2002], Saturn [e.g., *von Papen et al.*, 2014], and Mercury [*Uritsky et al.*, 2011]. In the Jovian magnetosphere, magnetic fluctuations in the ultralow frequency wavelength range do not show strong characteristic peaks as Pc and Pi pulsations often observed in the Earth's magnetosphere but rather broadband and turbulent features. Using Voyager flyby data, *Glassmeier* [1995] observed power law spectra of magnetic turbulence with an index of $\sim -5/3$ in the middle magnetosphere. Using magnetometer (MAG) data on board the Jovian magnetospheric orbiter Galileo, *Saur et al.* [2002] found a similar spectral index for the perpendicular components to the background field, while that of parallel component was found steeper (index ~ -2). The scaling was found independent of the radial distance in the middle magnetosphere at 6–26 R_J, where R_J is the Jovian radius of 71,492 km. The index -2 and the small-amplitude fluctuations with respect to the background field ($\delta b/B_0 \ll 1$) were used as arguments in favor of the weak turbulence theory of MHD turbulence to explain those observations [*Galtier et al.*, 2000]. *Russell et al.* [2000] showed that the transverse magnetic field component is larger than compressional component in lobe region and the two components become comparable in the current sheet. *Saur et al.* [2003] argued that the observed enhancement of the power of the fluctuations at 20–30 R_J [*Saur et al.*, 2002] provides Joule dissipation with electric potential along the magnetic field reaching ~100 kV, which is comparative with that required to accelerate electrons and to produce the Jupiter's main aurora. *Saur* [2004] studied the role of turbulence in heating the expanding magnetospheric plasma originated at Io.

Previous studies of turbulence in the Jovian magnetosphere have emphasized their power spectra and their spectral indices in a limited frequency range due to the low time resolution of the data ($\Delta t \approx 24$ s) used, although the Galileo/MAG measured the magnetic fluctuations with a higher time resolution ($\Delta t = 0.33$ s) within different regions of the magnetosphere. Combining both the low- and the high-time-resolution MAG data, we extend the previous studies of turbulence into a broader range of scales covering both MHD and kinetic scales of the Jovian magnetosphere. These scales correspond to observed frequencies on board the spacecraft of ~10^{-4}–1 Hz. We furthermore explore higher-order statistics to investigate intermittency. We use data from the Galileo plasma instrument (PLS) and from thermal/energetic particle models to investigate the possible relationship between the plasma characteristic scales and the observed spectral breaks. This paper is structured as follows: the observation and the data analysis method are described in section 2, followed by the results in section 3, and a discussion of limitations of the used data in section 4. Section 5 summarizes the main findings in the present study.

2. Data Description

Galileo is the first and, so far, the only Jovian magnetospheric orbiter that explored the Jupiter's magnetic equator for almost 8 years, from December 1996 to September 2003 (Figure 1). Since the Jupiter's magnetic axis is tilted by about 10° with respect to the rotation axis, the magnetosphere and its current sheet are flapping with the rotation period of 9 h and 55 min. Since the Galileo spacecraft is located near the Jovigraphic equator, it therefore passes through the plasma sheet and the lobe regions. The magnetospheric plasma is mainly composed of sulfur and oxygen ions originated from the moon Io. The magnetospheric plasma almost

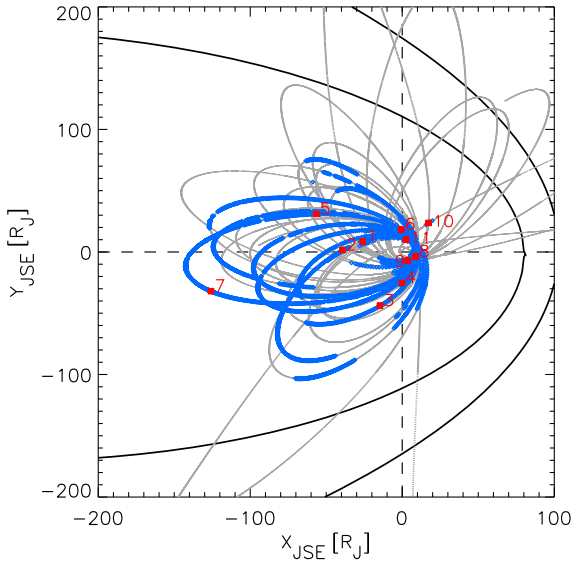

Figure 1. Galileo orbits (gray) and locations of low- (blue) and high-time-resolution (red squares) MAG data used in this study. The two black curves show the magnetopause and the bow shock positions from the empirical model of *Joy et al.* [2002]. The numbers in red represent the identification numbers of the high-time-resolution (HR) events.

corotates with Jupiter within 20 R_J, and the rotation motion continues in a vast region of the magnetosphere. The Galileo data set used in this study is taken from the NASA Planetary Data System (PDS) website.

2.1. The Magnetometer Data

The magnetic field data used in this study were measured by the fluxgate magnetometer (MAG) [*Kivelson et al.*, 1992]. The triaxial MAG instrument covers frequencies ranging from the DC up to a few hertz. Measurements with low time resolution (LR), $\Delta t = 4$–24 s, are available for several orbits covering various distances and local times (LTs) in the magnetosphere as shown in Figure 1. We use the data until orbit I25 because these orbits are entirely contained inside the magnetosphere, except for orbit C03 which would contain instrumental problem.

Several high-time-resolution (HR) observations are made by MAG during the magnetospheric survey and moon flybys. In order to focus on the magnetospheric turbulence, we do not use moon flyby events that include signatures of moon-magnetosphere interactions [e.g., *Kivelson et al.*, 2004]. Among the data measured over 23 periods, we analyze 11 events that have fluctuation amplitudes well above the noise level of the MAG instrument (described later in section 3.1). These events are marked by the red squares in Figure 1 and summarized in Table 1 including the observation time, the duration (it varies 35–120 min), and the mean ion plasma β. Events #1–5, #7, and #10 include plasma sheet intervals, event #6 is around the plasma sheet boundary, and events #8, #9, and #11 are close to Jupiter. Events #4 and #5 contain ~10,500 and ~8100 data points, respectively, in the lobe region and ~12,000 in the plasma sheet.

2.2. The Plasma Data

The plasma data used in this study (i.e., ion density, temperature, and velocity) come from the Galileo/PLS instrument [*Frank et al.*, 1992] for all events within a radial distance of 30 R_J. Beyond this radius, the PLS momentum data are not available. Therefore, we use the empirical axisymmetric model of *Bagenal and*

Table 1. Summary of High-Resolution Observations[a]

No.	Start Time (UT)	ΔT (min)	Number of Data Points	Galileo $(x,y,z)_{JSE}$ (R_J)	R (R_J)	LT (h)	β
1	06/30/1996 02:00	45.4	7,622	(−25.9, 8.57, 0.186)	27.3	22.7	2.3
2	09/11/1996 02:38	40.4	5,969	(−39.2, 1.5, −0.22)	39.3	23.8	1.7
3	03/30/1997 18:49	45.5	7,557	(−14.7, −43.9, −0.037)	46.3	4.7	3.4
4	05/06/1997 13:00	129.	12,158	(−0.2, −25.3, −0.38)	25.4	5.9	1.1
5	07/04/1997 14:09	117.	12,466	(−56.6, 30.9, −0.12)	64.6	22.0	3.6
6	07/28/1997 13:50	60.7	10,175	(−0.7, 18.2, −0.04)	18.3	18.1	1.0
7	08/23/1997 14:07	121.	21,594	(−125.8, −31.9, −0.52)	130.	0.9	21.
8	05/03/1999 15:59	121.	21,265	(8.5, −3.8, −0.02)	9.4	10.4	0.15
9	07/01/1999 23:52	114.	20,067	(3.6, −6.9, 0.00)	7.9	7.8	0.090
10	11/03/2002 15:27	35.0	6,308	(17.2, 23.5, −0.29)	29.2	15.5	2.4
11	11/04/2002 21:48	45.6	7,909	(2.4, 9.9, −0.12)	10.3	17.0	0.26

[a]Columns from left to right are the identification number (ID), the observation start time, the observation duration in minutes, the number of data points, the Galileo coordinates in the Jupiter Solar Equatorial (JSE) frame of reference and its radial distance from Jupiter in units of Jupiter radii $R_J = 71{,}492$ km, the local time in hour, and the ion plasma β. The latter four values are the mean value during each interval.

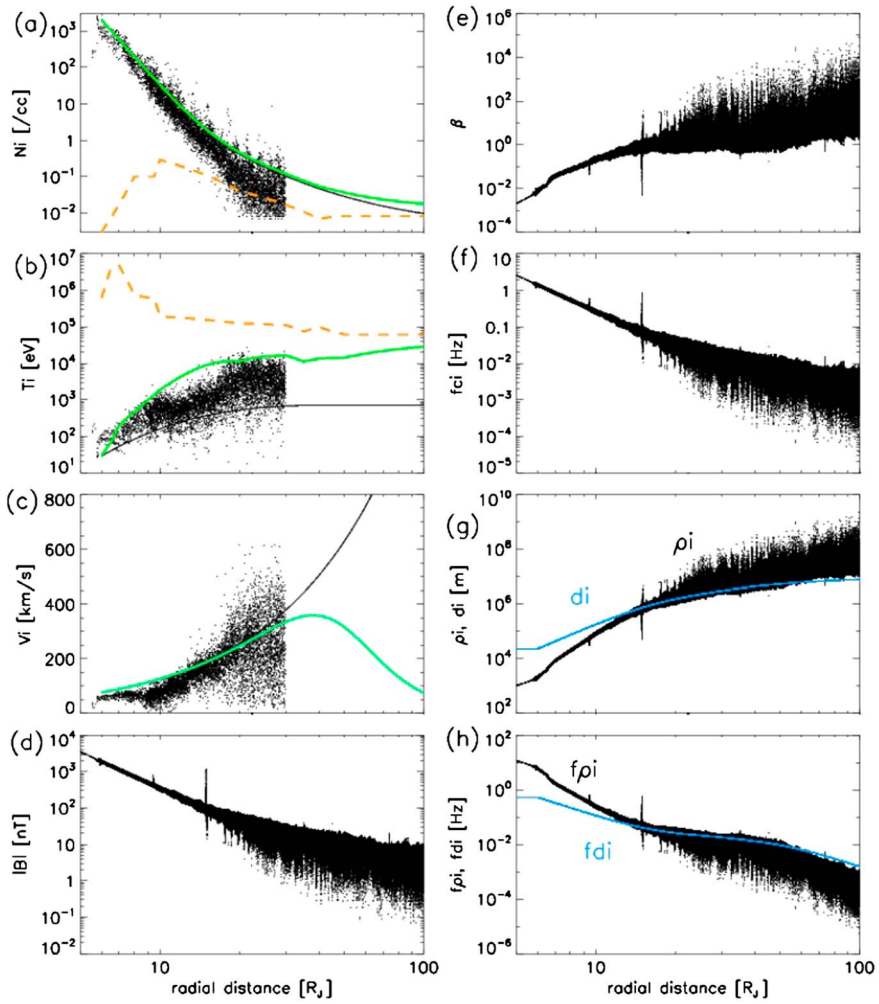

Figure 2. Radial profiles of (a) the ion density, (b) the ion temperature, and (c) the azimuthal velocity from PLS momentum data (black dots), (d) the magnetic field strength from MAG data, (e) the plasma β, (f) the ion cyclotron frequency, (g) the ion gyroradius (black dots) and ion inertial length (blue), and (h) Taylor-shifted ion gyroradius (black) and ion inertial length (blue). Figures 2a and 2b also show the thermal (black solid line) and the energetic plasma (dashed line) from the axisymmetric empirical models (see text) and their total average (green thick line). Figure 2c also shows the corotation velocity (black thin line) and the velocity profile of the corotation lag model (green thick line).

Delamere [2011] to estimate the ion density and temperature. In Figures 2a and 2b, the ion density and temperature from PLS observation are compared (as a function of radial distance) with those predicted by the empirical model. One can observe a relatively good agreement between the two observations for distances smaller than 30 R_J. This indicates that one can use this empirical model to extrapolate the data into the region where the spacecraft data are unavailable.

PLS measures particles within the energy range of 0.9 eV–52 keV. Since energetic particles play an important role for large radial distances [e.g., *Bagenal and Delamere*, 2011], we include in our study the effect of energetic particle referring to a model based on measurements by the energetic particle detector in the energy range of 50 keV–50 MeV [*Mauk et al.*, 2004]. Figures 2a and 2b show the thermal (black solid line) and energetic plasma (orange dashed line) from the model and their total average (green thick line). For the density, thermal particles are dominant while energetic particles start modifying the total density at large distance >50 R_J. Temperature increases by an order of 2 due to the energetic particles. In the following, we use the total density and averaged temperature.

The plasma corotates with Jupiter in the inner magnetosphere <20 R_J; however, the radially transported plasma cannot maintain the same corotation velocity at larger radial distance as observed by, e.g., *Krupp et al.*

[2001] and *Frank and Paterson* [2002]. Here the plasma lag from the corotation is modeled as a function of the radial distance r (R_J) as in *Cowley and Bunce* [2001]:

$$v_i/v_J = 1/\left(1 + (r/50)^4\right), \quad (1)$$

where v_i is the plasma velocity and v_J is the corotation velocity. This modifies the ion velocity to the profile shown in Figure 2c (green curve).

The previous magnetic (Figure 2d) and plasma (Figures 2a–2c) data are used to estimate the typical ion scales that will be compared to the spectral breaks observed on the magnetic energy spectra, namely, the ion cyclotron frequency $f_{ci} = qB/(2\pi\, m_{ion})$, the ion gyroradius $\rho_i = v_{th}/(2\pi\, f_{ci})$, and the ion inertia length $d_i = c/\omega_{pi}$. Here q is the electric charge, B is the magnetic field strength, m_{ion} is the ion mass, v_{th} is the ion thermal velocity, c is the speed of light, and ω_{pi} is the ion plasma frequency. The Jovian magnetospheric plasma is dominated by multiple-charged sulfur and oxygen ions. Measurements show large variation in the plasma composition. We use $q = 1$ and the mean ion mass $m_{ion} = 20$ in this study [e.g., *Thomas et al.*, 2004; *Radioti et al.*, 2005]. The latter two parameters are converted into related frequencies through the Taylor frozen inflow assumption, i.e., $f_{\rho i} = v_i/(2\pi\, \rho_i)$ and $f_{di} = v_i/(2\pi\, d_i)$, where v_i is the plasma velocity which is much larger than the spacecraft speed. These parameters are shown in Figures 2e–2h.

The Taylor hypothesis is generally questioned when the characteristic speeds of the fluctuations (the Alfvén speed $V_{Alfvén}$ or the sound speed C_s) become comparable to the flow speed v_i. However, it is important to emphasize that the Taylor assumption can be valid even when $v_i \sim V_{Alfvén} \sim C_s$. To assess its validity, it is indeed necessary to consider in more detail the equation relating the observed frequency onboard spacecraft and the one in the plasma rest frame: $\omega_{sc} = \omega + k\, v_i \cos\theta_{\mathbf{kv}}$. From this equation, it becomes clear that for Alfvénic turbulence $\omega \sim k_{//} V_{Alfvén}$ that is strongly anisotropic ($k_{//} \ll k$), the Taylor hypothesis is still valid even when $V_{Alfvén} \sim v_i$: $\omega_{sc} \sim k v_i\, (1 + k_{//} V_{Alfvén}/k v_i) \sim k v_i\, (1 + k_{//}/k) \sim k v_i$ (under the assumption $\cos\theta_{\mathbf{kv}} \sim 1$) [e.g., *Sahraoui et al.*, 2010]. Magnetosheath turbulence can also have nearly zero frequency in the plasma rest frame (although it could reach high frequency on board the spacecraft), as already shown for turbulence in the terrestrial magnetosheath using the Cluster multispacecraft data [e.g., *Sahraoui et al.*, 2006; *Mangeney et al.*, 2006]. Unambiguous tests of the validity of the Taylor hypothesis require multispacecraft observations, which are not currently available in planetary magnetospheres. Therefore, one must consider with some caution the estimated frequencies corresponding to the ion gyroradius and inertial length given in the paper, which are the only results in which the Taylor hypothesis is used.

3. Results

3.1. Statistics on Spectra

We first discuss the event labeled #5 observed on 4 July 1997. Figure 3 shows the waveforms and corresponding time-frequency spectrograms of the magnetic field for this event. Figure 3a shows a longer time period that includes the period when the HR data are available (central band, which is shown in Figure 3b). We use the radial (B_r), colatitudinal (B_θ), and azimuthal (B_ϕ) components of magnetic field waveforms in the Jupiter Solar Equatorial (JSE) spherical coordinate system. Galileo was first located in the south lobe (right before the event) as indicated by the negative B_r component and the plateau shape in $|\mathbf{B}|$ before −30 min. Then, Galileo entered into the plasma sheet around HR start time as indicated by decreasing $|\mathbf{B}|$ and the sign reversal of B_r, and then it reached the north lobe after 70 min. Therefore, Galileo observed the plasma sheet during the first half of this HR event and then the north lobe. The magnetic fluctuations of B_θ, B_ϕ, and $|\mathbf{B}|$ within the plasma sheet have larger amplitude than those in the lobe as can be seen in Figure 3b.

The mean magnetic field $\mathbf{B_0}$ is determined by 1 h running average of LR data, as shown by green line in Figures 3a and 3b. The fluctuating field $\delta\mathbf{B}(t) = \mathbf{B}(t) - \mathbf{B_0}(t)$ is then transformed into the mean field-aligned coordinate system, in which the z axis is aligned with the mean field $\mathbf{B_0}$. This allows us to decompose the signal into parallel $\delta B_{//}$ and two perpendicular components ($\delta B_{\perp 1}$ and $\delta B_{\perp 2}$). The power spectral densities (PSDs) of $\delta B_{//}$, $\delta B_{\perp 1}$, and $\delta B_{\perp 2}$ are estimated using a wavelet transform

$$W_i(t,\tau) = \sum_{j=1}^{N} \delta B_i(t_j)\, \frac{1}{\sqrt{\tau}}\, \psi^*\left[(t_j - t)/\tau\right] \Delta t, \quad (2)$$

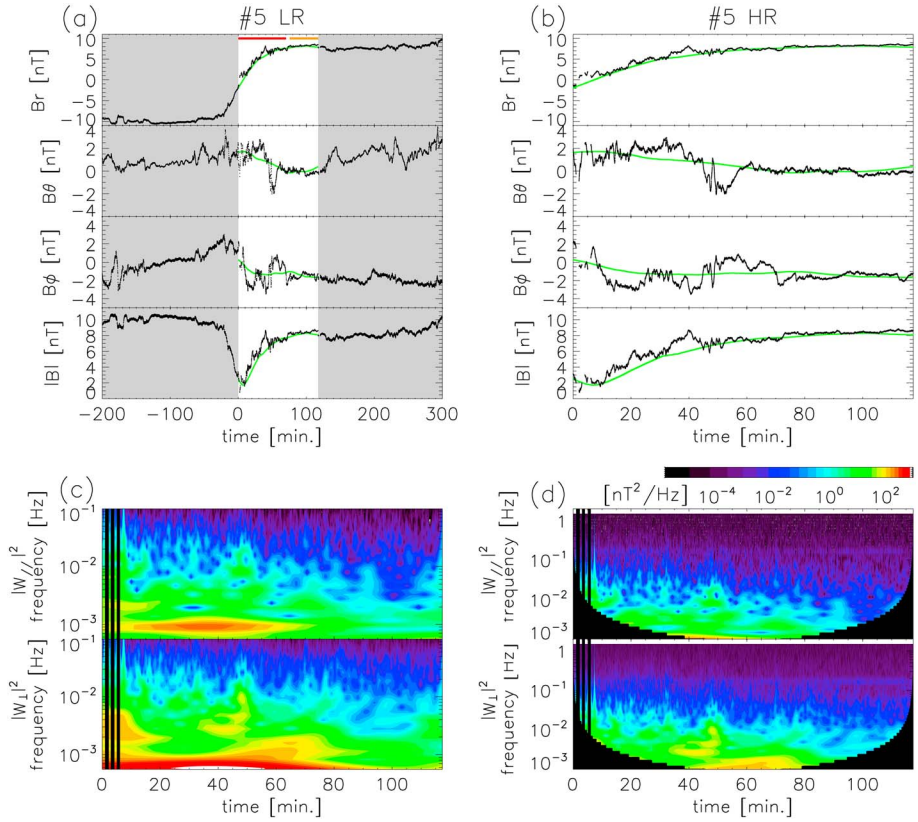

Figure 3. Magnetic field components and magnitude in (a) low time resolution (LR) and (b) high time resolution (HR) and the corresponding spectrograms of (c) LR and (d) HR (black hatches are caused by boundary effect) for event #5. Time "0" is the start time, i.e., 14:09 on 4 July 1997, of this HR event indicated by the white zone in Figure 3a. The green lines in Figures 3a and 3b are the mean magnetic field averaged over 1 h, and the red and orange horizontal lines in Figure 3a are plasma sheet and lobe crossing times.

as

$$\mathrm{PSD}_i(\tau) = \frac{2}{N\Delta t}\sum_{j=1}^{N} \Delta t \left| W_i(t_j, \tau) \right|^2, \tag{3}$$

where t is the time variable of N steps with interval Δt, τ is the time scale (i.e., the inverse of the frequency f), and ψ^* is the complex conjugate of the Morlet mother wavelet $\psi(u) = \pi^{-1/4} e^{i\omega_0 u} e^{-u^2/2}$ with $\omega_0 = 6$. Then the parallel spectrum density is obtained as $|W_{//}|^2$ from the wavelet transform of $\delta B_{//}$, the perpendicular spectrum density is obtained as $|W_\perp|^2 = |W_{\perp 1}|^2 + |W_{\perp 2}|^2$, and the total spectrum density is obtained as $|W|^2 = |W_{//}|^2 + |W_\perp|^2 = |W_{//}|^2 + |W_{\perp 1}|^2 + |W_{\perp 2}|^2$.

The spectrograms of the parallel and the perpendicular components are shown in the upper and lower plots of Figure 3c for LR data and those of Figure 3d for HR data. Similar features and quantities can be recognized in the power distributions of the LR and HR spectrograms for the frequency range where they overlap. Larger amplitude in the plasma sheet crossing can also be seen in the spectrograms in particular at low frequencies $<10^{-2}$ Hz. The perpendicular component has a larger power than the parallel component. The monochromatic signature seen near 0.1 Hz in Figure 3d (HR) would correspond to an overtone of the Galileo spin modulation about 19 s.

PSDs during the two intervals corresponding to plasma sheet and lobe crossing of event #5 are shown in Figures 4a and 4b, respectively. The LR and HR PSDs match quite well in the frequency range where they overlap, i.e., ~10^{-3}–10^{-1} Hz for this event. The difference becomes larger at the low-frequency part of the LR, which would be caused by several possible effects such as high- and low-pass filtering or the finite size sample effect. The perpendicular components (light blue and orange lines) are larger than the parallel one (green and yellow lines) up to the spectral break frequency f_b observed near 0.01 Hz, where a tendency

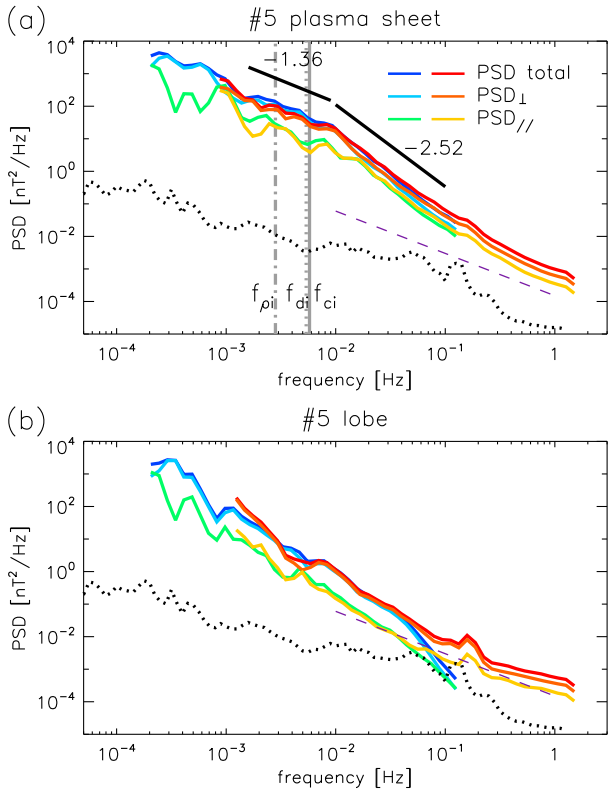

Figure 4. The spectra of the total, the perpendicular, and the parallel components from LR (blue green) and HR (red orange) for (a) plasma sheet crossing and (b) lobe crossing of #5 observation intervals. The solid black curves are the power law fits. The vertical solid, dash-dotted, and dotted lines indicate the ion cyclotron frequency f_{ci}, the Taylor-shifted gyroradius $f_{\rho i}$, and inertial length f_{di}. The dotted curve shows the noise level estimated from the observation data, and the dashed purple line is the prelaunch noise level for the dynamical range of ±32 nT case [*Kivelson et al.*, 1992].

toward power isotropization, i.e., $PSD_{\perp} \approx 2\,PSD_{//}$, can be seen. Linear fits of the total PSD on the log-log scale yield the slopes −1.36 and −2.52, respectively, below and above the break frequency f_b in the plasma sheet (Figure 4a). We note that in this study, we used power law fits of the magnetic energy spectra as usually done in turbulence studies, but this does not mean that all our data present the so-called inertial or dissipation ranges of solar wind turbulence. This caution should be kept in mind in particular for spectra measured in the lobe region, where the power law behavior is sometimes not clearly seen.

It is worth noting that all the spectra shown in Figure 4 lie above the estimated in-flight noise floor of the MAG instrument, indicated by the black dashed curves. The in-flight noise floor is estimated as the minimum PSD measured from 23 HR events and all LR data available in the lobes and in the solar wind. This spectrum would represent the upper bound of the real noise floor of the MAG instrument. The in-flight noise floor is estimated by, first, taking a running average over 300 time steps and then considering the minimum value of the average at each frequency for three dynamic ranges ($<\pm32$, $<\pm512$, and $<\pm16{,}382$) separately. The obtained noise is close to the prelaunch noise described in *Kivelson et al.* [1992]: 1×10^{-1}, 1×10^{-3}, $5\times10^{-5}\,nT^2\,Hz^{-1}$ at 1 Hz and $<1\times10^{-1}$, $<4\times10^{-2}$, and $<2\times10^{-2}\,nT^2\,Hz^{-1}$ at 0.01 Hz, for the dynamical ranges of ±16,384, ±512, and ±32 nT, respectively, as shown by purple dashed lines in Figure 4. The in-flight noise floor is lower than the laboratory one expected by *Kivelson et al.* [1992].

The PSDs in the plasma sheet and in the lobe exhibit different profiles as shown in Figures 4a and 4b: the PSDs in the lobe have lower amplitude and do not show any clear break in this event. The dominance of the perpendicular component extends to higher frequencies in the lobe (up to 0.1 Hz).

Figure 5a shows combined PSDs (thick lines) from those of LR and HR (thin lines) during plasma sheet (for $>18\,R_J$) and quasi-dipole region (for $<11\,R_J$) intervals of each HR period. Some LR spectra, i.e., #1, #2, #4, #6, #8, and #9, show discrepancies with the HR ones at high frequency. This may be due to low-pass filtering of the signal during the calibration procedure. The linear fits of the log-log plot show that the slopes at low frequency vary from −0.6 to −1.9 and those at higher frequency vary from −1.7 to −2.5. The slopes at low frequency of #7, #3, #2, #4, #8, and #9 are close to −1, which, by analogy with solar wind turbulence, may indicate that this range of frequencies corresponds to the "energy-containing scales" rather than to the classical inertial range of Kolmogorov turbulence. We note that these events are all observed when Galileo was located at the dawnside of the magnetotail region (LT = 23–24 h and 0–11 h). In other cases, the slopes in the low-frequency range vary from −1.3 to −1.9, which are closer to the Kolmogorov index; the spectra become steeper above the spectral breaks. The histograms of the spectral indices are shown in Figure 5b.

In order to identify the possible physical scale that would correspond to the observed spectral breaks, we plot in Figure 6a the correlations between the frequencies of the breaks and those characterizing the ion dynamics,

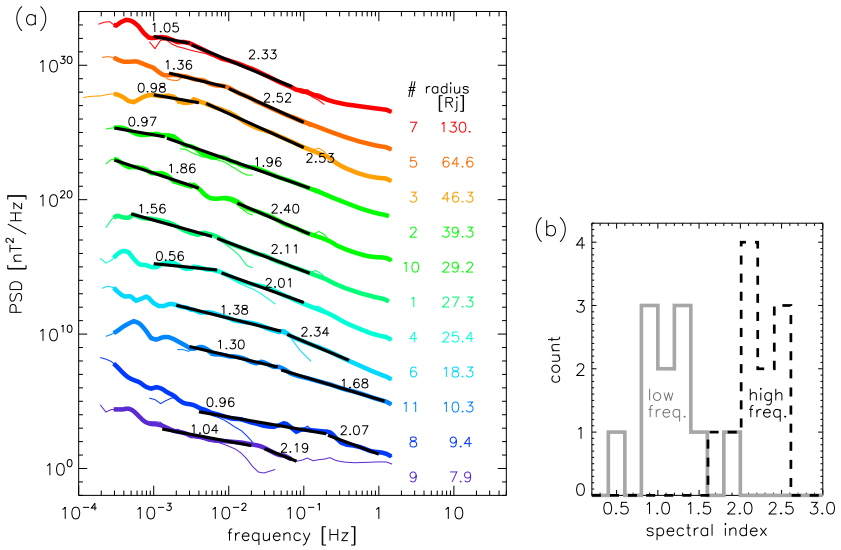

Figure 5. (a) PSDs of *B* (thick lines) combining HR and LR data (thin lines) during plasma sheet (for >18 R_J) and quasi-dipole region (for <11 R_J) intervals of each HR period, ordered from bottom to top by the radial distance given in the right-hand second column. Events ID are given in the first column. The PSDs are shifted up by $10^{(3k)}$, where k=0 for #9, k=1 for #8, ..., up to k=10 for #7, for clarity of the plot. The thick black lines are the corresponding power law fits. (b) The histogram of the spectral indices at low (gray solid line) and high (black dashed line) frequency ranges.

namely, the ion cyclotron frequency f_{ci} and the Taylor-shifted gyroradius $f_{\rho i}$ and inertial length f_{di}. A higher correlation coefficient (0.8) is found with the ion cyclotron frequency. This suggests the possible presence of high-frequency waves ($f \simeq f_{ci}$ in the plasma rest frame) and consequently the relevance of the ion cyclotron resonance as a mechanism of energy dissipation in these observations [*Goldstein et al.*, 1994]. In Figures 6b and 6c, we further investigate the problem of the relevant scale as a function of the plasma β. Both the plasma sheet (diamonds) and the lobe (plus signs) events are included. These events are chosen from the first orbits G01–G08 (except orbit I03). No significant difference in the correlation with $f_{\rho i}$ and f_{di} is found. Note that for high β events, no correlation is found with either $f_{\rho i}$ or f_{di}. A possible explanation of this might be the high uncertainties in the estimated plasma parameters as discussed in section 4.

3.2. Magnetic Compressibility

To identify the nature of the plasma modes involved in the observed turbulence, we use the magnetic compressibility, which is shown theoretically to be different for Alfvén and magnetosonic linear modes [*Gary et al.*, 2010; *Sahraoui et al.*, 2012]. It was also used recently to identify KAW turbulence in the solar wind [*Podesta and TenBarge*, 2012; *Kiyani et al.*, 2013]. The magnetic compressibility is defined as

$$C_b(\tau) = \frac{1}{N}\sum_{j=1}^{N} \frac{\left|W_{//}(t_j,\tau)\right|^2}{\left|W(t_j,\tau)\right|^2}. \quad (4)$$

Figure 7 shows the obtained magnetic compressibilities during plasma sheet (for >18 R_J) and quasi-dipole region (for <11 R_J) intervals of each HR period as a function of frequency normalized by f_{ci}. They show the trend of large value ≈0.5 at low frequency <0.1 f_{ci} and become smaller, ≈0.3, around f_{ci} and almost isotropic ≈0.33 at high frequency >10 f_{ci}, with large variation between the different intervals, in particular those at large radial distances. We emphasize that at large radial distances, the magnetic fluctuations become large with respect to the mean field, which would make it difficult to determine the background field and its direction with the method used here. Techniques based on the local field (i.e., scale dependent) decomposition are needed in this case [*Kiyani et al.*, 2013].

3.3. Intermittency and Higher-Order Statistics

In this section, we extend the turbulence analysis to higher-order statistics of the turbulent fluctuations to investigate their intermittent nature. Intermittency can be evidenced as heavy tails in the probability

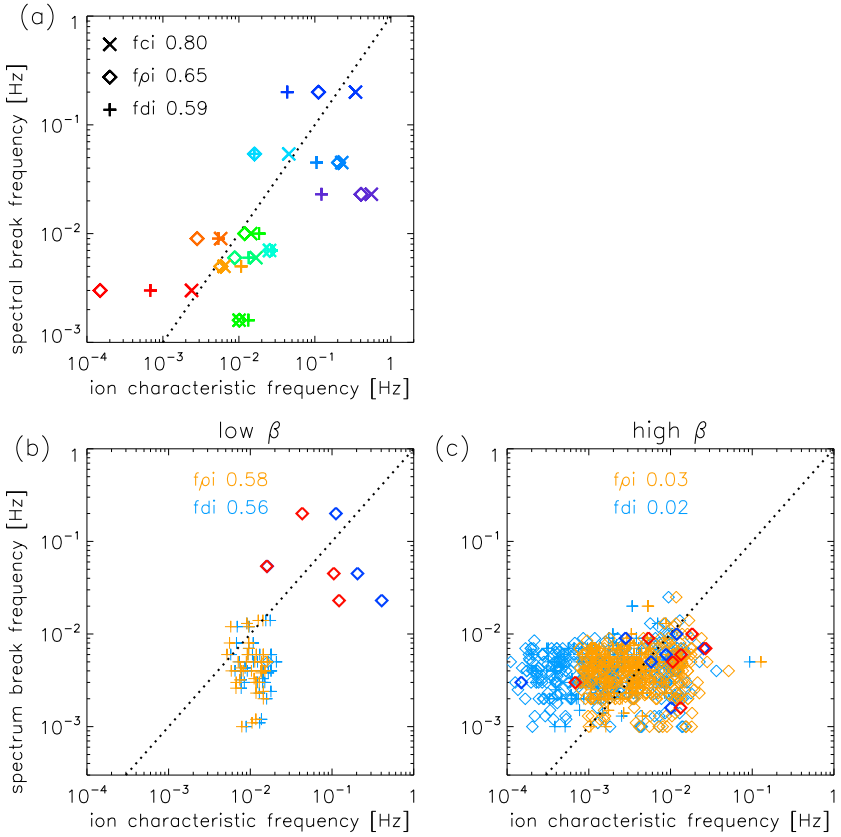

Figure 6. (a) Scatterplot of the spectral break frequencies as a function of the ion cyclotron frequency f_{ci} (crosses) and the Taylor-shifted gyroradius $f_{\rho i}$ (diamonds) and inertial length f_{di} (plusses) for 11 HR events (the color code is the same as in Figure 5). The scatterplots of spectral break frequency as functions of Taylor-shifted ion gyroradius $f_{\rho i}$ (orange and red) and inertial length f_{di} (blue) for (b) low and (c) high β cases are shown. The logarithmic correlation coefficients between spectral break frequency and the ion characteristic frequencies are labeled in each plot. For Figures 6b and 6c, the observations in the plasma sheet and the lobe regions are shown by diamonds and plus signs, respectively, and the thick symbols are those from HR data. The black dotted line indicates the correlation 1.

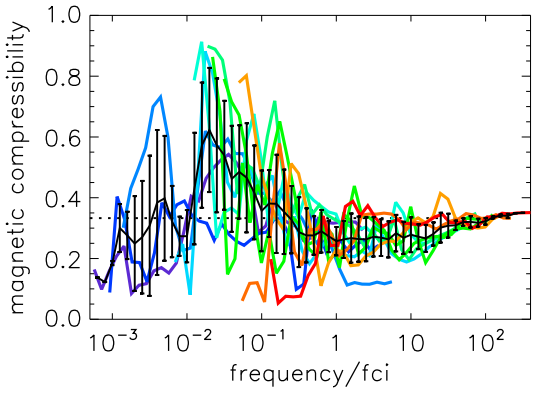

Figure 7. Magnetic compressibility as a function of the frequency normalized by f_{ci}. The color code and time interval are the same as in Figure 5a. The horizontal dotted line indicates power isotropization (~0.33), while the black solid line shows the mean value with associated statistical error.

distribution function (PDF) of the increments $\delta B_i(t,\tau) = \delta B_i(t+\tau) - \delta B_i(t)$. It can be estimated by computing higher moments (>2) of the PDFs or, equivalently, by estimating the different orders of the structure functions (SFs). The mth order of SF is given by

$$S_i^m(\tau) = \frac{1}{N}\sum_{j=1}^{N} \left|\delta B_i(t_j,\tau)\right|^m. \quad (5)$$

If $S_i^m(\tau) \propto \tau^{\zeta(m)}$, then one can estimate the scaling exponent $\zeta(m)$. A linear (respectively, nonlinear) scaling of $\zeta(m)$ with respect to m indicates a monofractal (respectively, multifractal) behavior of the turbulent fluctuations. The flatness (or the kurtosis) is often used as an alternative measure of intermittency. It is defined as

$$F_i(\tau) = \frac{S_i^4(\tau)}{\left\{S_i^2(\tau)\right\}^2}. \quad (6)$$

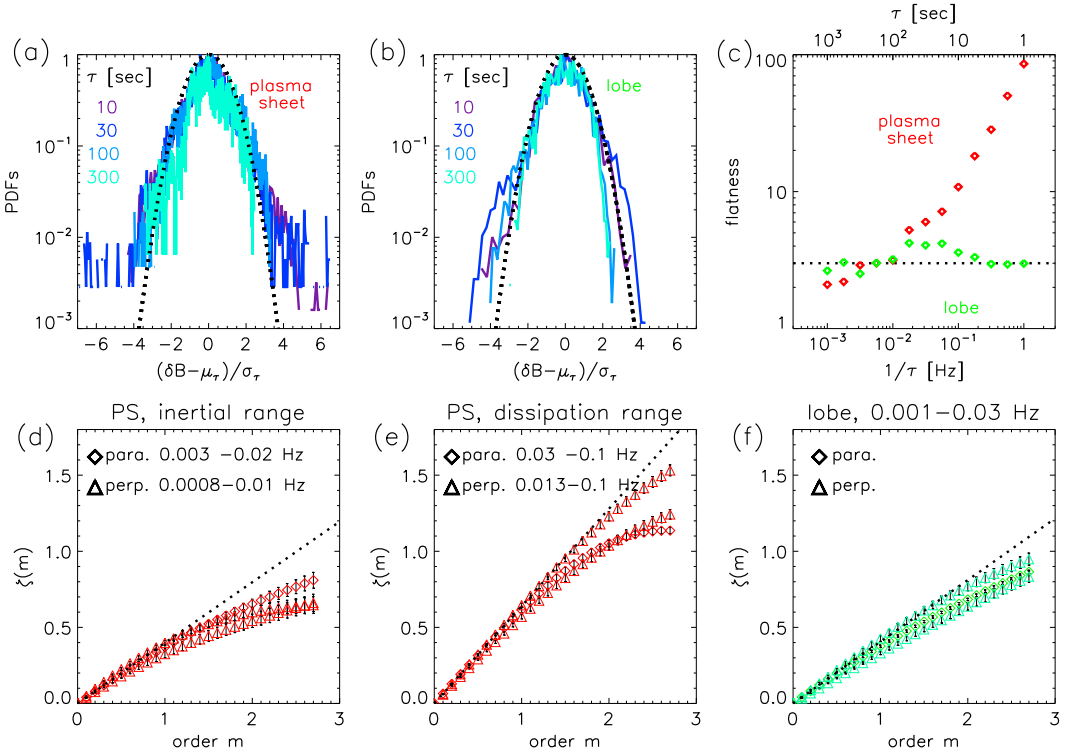

Figure 8. Probability distribution functions (PDFs) of (a) plasma sheet and (b) lobe crossing intervals of HR #5 for several time lags τ. A Gaussian PDF is plotted for comparison (dotted curve). (c) Mean flatness $(F_r + F_\theta + F_\phi)/3$ as a function of τ for the plasma sheet (red) and the lobe (green) intervals. The horizontal dashed line shows the Gaussian value of 3. Scaling exponents of structure functions in parallel (diamond) and perpendicular components (triangle) of (d) "inertial" and (e) "dissipation" ranges during plasma sheet and (f) lobe crossings. The dotted linear line shows monofractal case for comparison.

A monotonically increasing flatness at small scales indicates intermittent fluctuations. Note that a Gaussian PDF has flatness equal to 3, a property that can be easily shown from equation (6). We restrict the computation to orders $\leq$4 due to the limited number of data points, which makes the estimation of higher-order SFs unreliable [*Dudok de Wit*, 2004].

Figure 8a shows the centered and normalized PDFs of the increments of the magnetic field magnitude δB for different time lags τ during plasma sheet crossing (μ_τ and σ_τ were obtained from a Gaussian fitting function). The PDFs for $\tau = 100$ s and 300 s are almost Gaussian as shown by the dotted lines and depart from gaussianity for smaller values of τ ($\tau = 10$ s and 30 s). The PDFs in the lobe (Figure 8b) show only small deviations from a Gaussian PDF, as confirmed by the flatness shown in Figure 8c. It is indeed found to be close to 3 except near $\tau = 30$ s where it increases to 4, then it decreases to 3 again for smaller values of τ. This would reflect reaching the noise floor of the instrument [*Kiyani et al.*, 2013]. On the other hand, the flatness obtained in the plasma sheet increases with decreasing τ, indicating the presence of intermittency.

The previous results are confirmed by computing the scaling exponents of the SFs defined in equation (5). Figures 8d–8f show the scaling exponent $\zeta(m)$ from the inertial (0.003–0.02 Hz for parallel and 0.0008–0.01 Hz for perpendicular) and the dissipation (respectively, 0.03–0.1 and 0.013–0.1 Hz) ranges in the plasma sheet and from the 0.001–0.03 Hz range in the lobe, respectively. Multiexponent scaling is found for all plots, with large differences between perpendicular (triangle) and parallel (diamonds) components in the plasma sheet and less deviation from monoexponent scaling in the lobe case.

The flatness of the 11 HR events during plasma sheet (for $>18\ R_J$) and quasi-dipole region (for $<11\ R_J$) intervals are shown in Figure 9. Most events show large (>6) and increasing flatness at small scales, which confirms the intermittent nature of the turbulence. However, a few events show decreasing intermittency at small τ, which can be explained by approaching the noise floor of the MAG instrument.

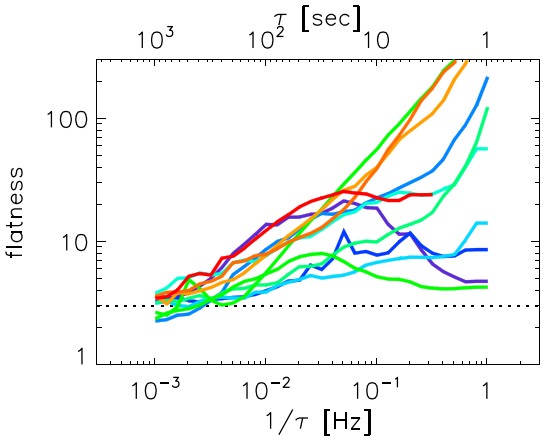

Figure 9. Mean flatness as a function of the inverse of the time lag τ for 11 HR events. The color code and time interval are the same as in Figure 5a. The horizontal line shows the flatness for Gaussian case (=3).

3.4. Dependence on the Radial Distance and on the Local Time

Since the HR data are not always taken, we investigate the generality of turbulence properties reported above using LR data measured at different LT and distances from the planet. In this analysis, we bin the data into 16 radial distances as 20–25, 25–30, …, 45–50, 50–60, 60–70, …, 130–140, and >140 R_J. In addition, we investigate the plasma sheet and the lobe regions separately. Accurate separation between the two regions requires particle data as well, but here we distinguish them using the magnetic field waveforms only. First, we choose the time interval (t_{j-1}, t_j) when $|\mathbf{B}| > 0.6\ |\mathbf{B}|_{1\ h}$, where $|\mathbf{B}|_{1\ h}$ is 1 h running average of $|\mathbf{B}|$, at a radial distance greater than 20 R_J. If this interval $tj - tj_1$ is greater than 90 min and less than three rotation time (1785 min), we set two intervals, (t_{j-1} + 40 min, t_j − 40 min) and (t_j − 40 min, t_{j+1} + 40 min], for the crossing times of the lobe region and the plasma sheet, respectively. In order to avoid sinusoidal field variations in the plasma sheet, which is often observed in the duskside and can be detected as lobe in the above procedure, we added an additional criterion for the lobe detection: {max($|\mathbf{B}|$) − min($|\mathbf{B}|$)}/median($|\mathbf{B}|_{1\ h}$) < 0.4 during the time interval (t_{j-1} + 40 min, t_j − 40 min).

Figure 10a shows the PSD in the plasma sheet for each bin. All PSDs decrease with frequency; the largest powers are observed for small distances from the planet. Figures 10b–10d show the mean profiles of PSDs after normalizing their frequency by f_{ci}, $f_{\rho i}$, and f_{di} at their observation points. The case with a normalization by f_{ci} shows less scatter for different radial profiles (Figure 10b), compared to those with

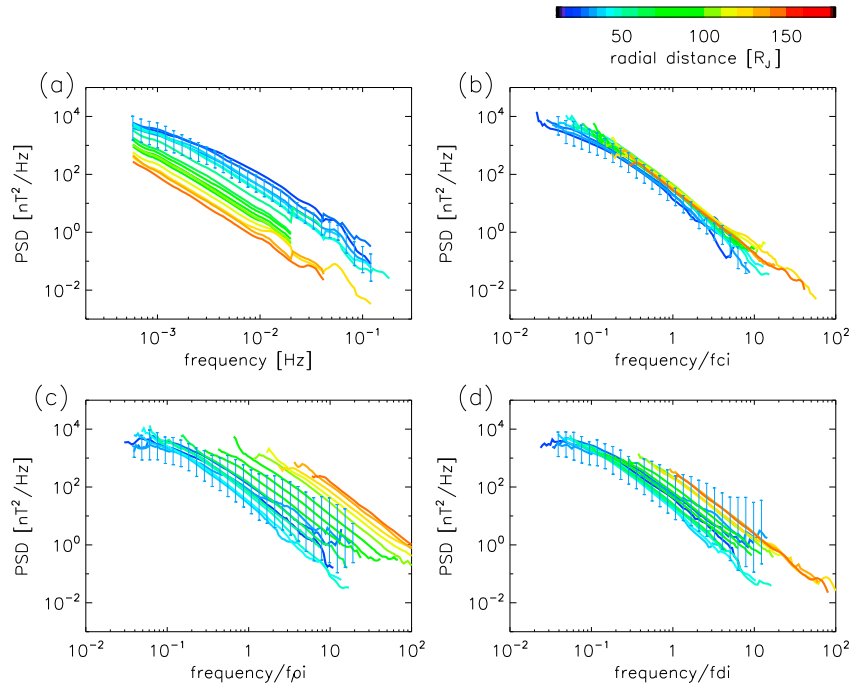

Figure 10. Total power spectra of low-resolution data taken in the plasma sheet averaged over 16 radial bins as functions of (a) the frequency and of the frequencies normalized by (b) f_{ci}, (c) $f_{\rho i}$, and (d) f_{di}. The corresponding radial distance is shown in color bar. Statistical variance is added as error bars for one radial case for a reference.

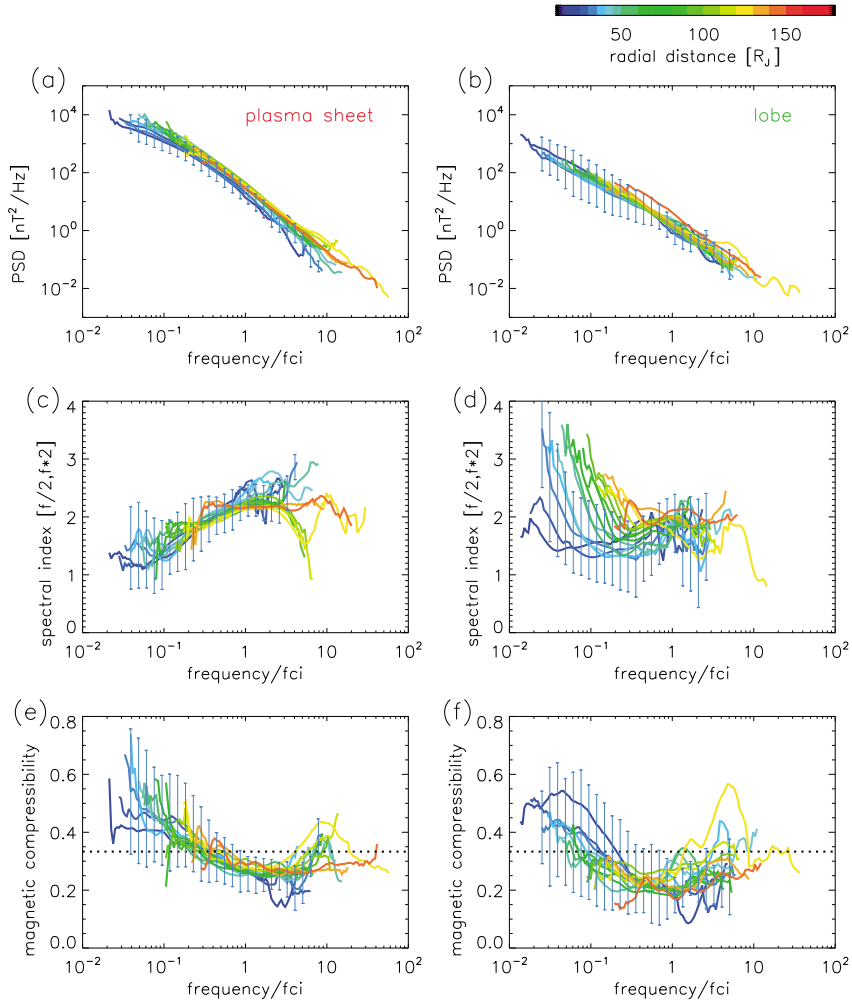

Figure 11. (a) The total power spectra, (c) spectral indices, and (e) magnetic compressibilities of low-time-resolution data observed in the plasma sheet averaged over 16 radial bins as a function of frequency normalized by f_{ci} and (b, d, and f) those observed in the lobe, respectively. The corresponding radial distance is shown in color bar. Statistical variance is added as error bars for one radius case for a reference. The horizontal dotted line in Figures 11e and 11f indicate the power isotropization level (~0.33).

normalizations by f_{pi} and f_{di}. This suggests a strong correlation between the fluctuation amplitudes and the background (i.e., mean) magnetic field.

The PSDs observed in the plasma sheet (Figure 11a) are larger than those in the lobe (Figure 11b). We estimated the scaling dependence as a function of frequency using a running slope method: the spectral index first calculated in the frequency range of ($f_c/2$, $2f_c$) and attributed to central frequency f_c of the interval. Then, the frequency f_c is shifted to span all the frequency range. Note that sudden changes in spectral slope at a certain frequency are smoothed out in this method. The spectral indices in the plasma sheet (Figure 11c) and in the lobe (Figure 11d) are shown as a function of the frequency normalized by f_{ci}. This normalization provides similar profile for the plasma sheet $<100\,R_J$ cases with an increase from 1.5 at $f/f_{ci}=0.1$ to >2 at $f/f_{ci}=1$. The spectral indices in the lobe region show a large variance and have no clear trend. The magnetic compressibility also decreases until power isotropy is achieved at high frequency for both the plasma sheet (Figure 11e) and the lobe cases (Figure 11f). The magnetic compressibility near f_{ci} seems smaller in the lobe than in the plasma sheet, in agreement with the PSDs shown in Figures 4a and 4b.

The flatness in the plasma sheet and in the lobe regions estimated from the whole data interval at each radial bin increases with frequency as shown in Figures 12a and 12b, respectively, while they do not show clear

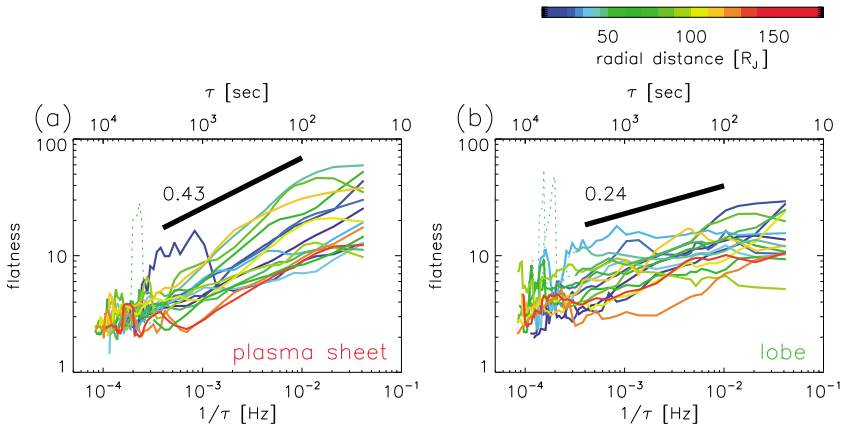

Figure 12. Flatness observed in (a) the plasma sheet and (b) lobe regions, within each 16 radial bins as a function of the time lag τ. The corresponding radial distances for the solid lines are shown as a color bar. The black thick line shows the flatness slope in the range of $100 < \tau < 2500$ s, averaged over all radial distances in each region. The large value at τ~5000 shown by the dotted line would be statistically less reliable.

dependence on the radial distance. The slope of the flatness in the scale range 100 s $< \tau <$ 2500 s (black thick line) in the plasma sheet, 0.43 ± 0.22, is larger than in the lobe, 0.24 ± 0.17. The deviation from three of the Gaussian case is more prominent in the current sheet.

Figure 13a shows the PSDs in the plasma sheet and in the lobe at two frequencies, 0.3 f_{ci} (crosses) and f_{ci} (diamonds), which are covered by various radial bins, as a function of the radial distance. As seen in Figures 11a and 11b, the plasma sheet PSDs show larger power of the fluctuations than those in the lobe for almost all radial distances. As in Figure 10b, the power densities normalized by f_{ci} show smaller variation with the radial distance. In the plasma sheet, they show an enhancement trend at 45–50 R_J and around 100 R_J. In the lobe region, the PSDs also show small enhancement trend near 45–50 R_J at f_{ci}, while they increase with radial distance at 0.3 f_{ci}. In Figures 13b and 13c, we split the data into dawnside (LT 0–12 h, orange) and duskside (12–24 h, blue), both in the plasma sheet and in the lobe regions. In the plasma sheet, the PSDs in the duskside are larger than those in the dawnside at $<$50 R_J, while the PSDs in the dawnside are larger than that in the duskside at $>$80 R_J. There is no clear difference between the dawnside and the duskside in the lobe region.

4. Discussion and Limitations of the Used Data

The results reported in the previous sections should be viewed within some limitations of the data used. Below, we discuss some of these limitations with their possible implications on the reported results.

The estimation of the ion characteristic scales involves several assumptions: (i) An empirical model in the plasma sheet [*Bagenal and Delamere*, 2011] is used to estimate the plasma moments when the PLS data were unavailable. A comparison between the observations and the model indicates possible modification of $f_{\rho i}$ and f_{di} by a factor of 3. The same modification factor of $f_{\rho i}$, f_{di}, or β is also obtained from estimating energetic particle parameters using the empirical model. (ii) Assumed mass and charge of ions influence ion characteristic frequencies directly in addition to their effects on plasma momentum estimation. The mean ion mass m_{ion} considered here is 20 due to oxygen and sulfur ions with ion charge $q = 1$. Since $f_{\rho i}$ and f_{di} are proportional to $q(m_{ion})^{-1/2}$, the estimated ion values are 22% of that of protons. Since f_{ci} is proportional to $q(m_{ion})^{-1}$, the estimated f_{ci} is 5% of that of protons. Sulfur and oxygen ions with $q \geq 2$ are also frequently observed at 0.6–60 keV/q in the middle and outer magnetosphere [*Geiss et al.*, 1992]. (iii) The Taylor hypothesis is used for $f_{\rho i}$ and f_{di} estimations in this analysis: its strict evaluation requires multispacecraft data, which are currently unavailable in planetary magnetospheres.

The Jovian magnetosphere allows us to explore a wide range of values of the plasma β, typically $10^{-1} < \beta < 10^3$ at large radial distance $>$20 R_J (Figure 2e), in comparison with $0.5 < \beta < 2$ in the solar wind at 1 AU [*Sahraoui et al.*, 2013], $10^{-1} < \beta < 10$ in the Earth's magnetosphere, and $0.04 < \beta < 1$ in the Saturn's magnetosphere [*von Papen et al.*, 2014]. Using the relation $\beta = (f_{di}/f_{\rho i})^2$, one obtains the ratio $0.32 < f_{di}/f_{\rho i} < 32$ in the Jupiter's

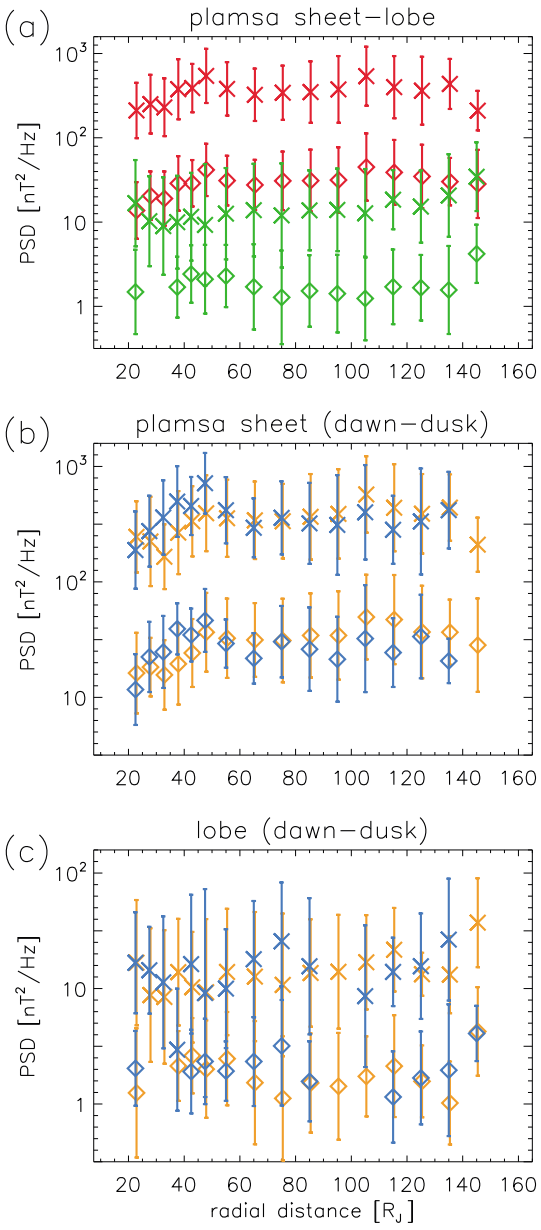

Figure 13. Radial profiles of the total PSD observed (a) in the plasma sheet (red) and in the lobe (green) regions for two selected frequencies 0.3 f_{ci} (crosses) and f_{ci} (diamonds) and comparisons between dawnside (orange) and duskside (blue) (b) in the plasma sheet and (c) in the lobe regions. The error bars corresponds to the variance at each radial bin.

magnetosphere. This large separation between the ion gyroradius and inertial length scales should make it easy to distinguish between the two scales in the observations presented here. However, no significant difference in the correlation between these two scales and the break frequencies was found. This may indicate high uncertainty in estimating these scales from observations as we discussed it above. For example, the shifting trend toward large frequencies for large radial distances in Figures 10c and 10d might stem from an overestimation of the mean ion mass in the outer magnetosphere, where solar wind-originated proton ratio would increase. Higher ion charge at larger radial distance [*Geiss et al.*, 1992] also has the similar effect. Other plasma parameters involving density and temperature are subject to higher uncertainty than f_{ci}, which is affected only by the errors in q and m_{ion}. Better particle measurements are expected from the future European Space Agency mission JUICE.

The 11 HR events analyzed in this study have $3\,\text{nT} < |\mathbf{B}| < 740\,\text{nT}$, which corresponds to $0.002 < f_{ci}$ ($m_{ion} = 20$) < 0.6 Hz and $90\,\text{Hz} < f_{ce} < 20$ kHz, where f_{ce} is the electron cyclotron frequency. Since the MAG data cover the frequency range ~10^{-4}–1 Hz, one can use these data to study both MHD and ion kinetic scales. Analyzing smaller (i.e., electron) scales requires using the search coil data of the Galileo plasma wave science, which covers the frequency range of 5.6 Hz–75 kHz. This study is postponed to a future work.

A question that has not been addressed in this paper is about the trigger of the observed turbulence. Previous surveys found a good correlation between the enhancement of the ultralow frequency waves in the magnetosphere and the solar wind dynamical pressure [*Hanlon et al.*, 2004; *Tao et al.*, 2005]. Note, however, that turbulence nature of HR events investigated here does not show clear dependence on the solar wind variation estimated from one-dimensional MHD model as in *Tao et al.* [2005]. Fast plasma flow and its velocity shear with surrounding plasma, as well as local instabilities [e.g., *Sahraoui et al.*, 2004, 2006], are believed to play a key role in generating turbulence in the terrestrial magnetosphere. Investigating the time dependence of the turbulence activity and its connection with the variation of the solar wind dynamics is an important question that would help in understanding the radial dependence of the turbulence properties found in this study. This work is also planned in the near future.

5. Major Results and Conclusions

Using the Galileo MAG high- and low-time-resolution data, the plasma data from the PLS instrument, and empirical models of the Jovian magnetosphere, we analyzed the properties of the magnetic turbulence at

MHD and kinetic scales in different regions of the Jovian magnetosphere. Several important results were found in this statistical study. They can be summarized as follows.

5.1. Spectral Features

Most of the PSDs in the plasma sheet were found to have a spectral break in the frequency range 10^{-3}–0.3 Hz. The frequencies of the breakpoints were found to better correlate with the local ion gyrofrequency, rather than with the ion spatial scales ρ_i or d_i (Figure 6a), within the limitations discussed above. Less scatter in the statistical results was indeed found when the frequency is normalized to the ion gyrofrequency as in Figures 10b, 11c, and 11e. This contrasts with the solar wind case where good correlation with the ion inertial scale has been reported [*Perri et al.*, 2010; *Bourouaine et al.*, 2012]. This suggests the possible role of the ion cyclotron waves and resonance in the dissipation of magnetic energy into particle heating. Power law fits of the PSDs below and above the spectral breaks show that the spectral indices vary within the intervals −0.6 to −1.9 and −1.7 to −2.5, respectively. Spectra with slope close to −1 in the lower frequency range are all observed in the dawnside magnetotail.

5.2. Nature of the Turbulent Fluctuations

The perpendicular component of the PSDs is dominant at low frequency before power isotropy is recovered at high frequencies. Larger magnetic compressibility is observed in the plasma sheet (Figures 4a and 11e) than in the lobe (Figures 4b and 11f), which is consistent with the enhanced power in the near-equator region with a more compressible component at low frequency as reported by *Russell et al.* [2000]. The steeper spectra in the parallel direction than in the perpendicular one reported by *Saur et al.* [2002] would also reflect large decrease in the parallel component. Average magnetic compressibility of about 0.5 (with large variance though) was observed at MHD scales, then it decreases to 0.2–0.3 within the kinetic range (Figure 11e). This behavior is in agreement with recent observations in the Saturn's magnetosphere [*von Papen et al.*, 2014]. Both contrast with the magnetic compressibility reported in the solar wind, known to be consistent with the KAW turbulence [*Podesta and TenBarge*, 2012; *Kiyani et al.*, 2013]. Comparing to the theoretical prediction by *Sahraoui et al.* [2012], the observed compressibility lies between those of the Alfvén mode ($C_b = 0$) and the magnetosonic modes ($C_b = 1$), while at small scale, an isotropization of the power is observed in the data ($C_b = 1/3$). This suggests the possible coexistence of both Alfvénic and magnetosonic fluctuations in the Jovian magnetosphere.

5.3. Intermittency

Intermittency is a general feature associated with turbulence in magnetized plasmas. In the Jovian magnetosphere, observations show different localized structures, e.g., plasma sheets and discontinuities, which appear as non-Gaussian tails in the PDFs of the magnetic field increments (Figures 8, 9, and 12). This feature is more prominent in the plasma sheet, where magnetic reconnection possibly occurs, than in the lobe. The slope of flatness in the plasma sheet, ~0.4, is a slightly steeper than that in the plasma sheet (~0.3) of the Saturn's magnetosphere [*von Papen et al.*, 2014]. In the terrestrial magnetosphere, intermittency is largely seen in the central plasma sheet, and it decreases when moving to outer plasma sheet and to the lobe region during plasma fast flow events [*Weygand et al.*, 2005]. Development of multifractality of the turbulent fluctuations in the sub-MHD scales was also seen in the terrestrial thick plasma sheet when bursty bulk flow is observed [*Vörös et al.*, 2004b]. Our observations show a similar spatial trend, which may be related to the fast plasma flows and the resulting radial dependence of the power of the fluctuations.

5.4. Spatial Distribution and Relation With Magnetospheric Dynamics

In the plasma sheet, the PSDs in the duskside were found larger than in the dawnside for distances $<50\ R_J$ and inversely for distances $>80\ R_J$. Distances $<50\ R_J$ correspond to regions where corotation lag increases and where the magnetosphere-ionosphere coupling transfers angular momentum to accelerate the plasma into the planetary rotation. In addition to this rotation-dominant and axisymmetric system, the boundary with the solar wind in the dayside adds a dawn-dusk asymmetry, as observed by Galileo [*Krupp et al.*, 2001]. In the duskside, the flux tubes compressed in the confined noonside drift toward the vast nightside, experiences expansion in the radial direction, and the bend-back feature would increase. This effect is clearly illustrated in global magnetospheric simulations [e.g., *Miyoshi and Kusano*, 2001; *Ogino et al.*, 1998; *Chané*

et al., 2013]. This increase of the flow shear in the duskside would cause the enhancement of the fluctuation power for distances $<50\ R_J$, which in turn would affect the scaling of the energy spectra.

On the dawnside, Galileo observations showed the presence of periodic flow bursts of energetic particles in the radial direction in the Jovian magnetotail at distances $>50\ R_J$ [*Woch et al.*, 2002]. These events occur periodically and are interpreted as reconnection processes involving a magnetotail reconfiguration. As for the Earth, they occur in the confined plasma sheet which is observed on the Jovian dawnside. *Kronberg et al.* [2005] suggested that the driving mechanisms could imply the plasma loading of fast-rotating flux tubes associated with centrifugal forces rather than solar wind-magnetosphere interactions in the terrestrial case. North-south magnetic field events associated with density decrease are dominant in the dawnside of the nightside magnetosphere. The density drop suggests lobe reconnection [*Kasahara et al.*, 2011, 2013]. In all cases, the energy released by these processes would enhance the turbulent power in the plasma sheet at large radial distances ($>50\ R_J$) in the dawnside. This would also be related to the small spectral slopes close to -1 in the "energy-containing scales" observed in the dawnside magnetotail (section 3.1 and Figure 5). These results also support the suggestions by *von Papen et al.* [2014] in the case of Saturn that large slope variation in the low-frequency range is due to the magnetospheric dynamics.

Acknowledgments

We acknowledge the working teams and PIs of Galileo instruments and Planetary Data System (PDS) website system. C.T. thanks K.K. Khurana, M.G., Kivelson, J.M. Weygand, and K. Kiyani for their useful discussions and data technical information. This work was supported by Ecole Polytechnique, partly by a grant-in-aid for Scientific Research from the Japan Society for the Promotion 541 of Science (JSPS), and by the ANR project THESOW (grant ANR-11-JS56-0008). J.D.P. was funded at LPP through the ANR project THESOW (grant 11-JS56-0008). The data used for this paper are all available at the NASA's PDS website (http://pds.nasa.gov/).

Michael Liemohn thanks the reviewers for their assistance in evaluating this paper.

References

Alexandrova, O., and J. Saur (2008), Alfvén vortices in Saturn's magnetosheath: Cassini observations, *Geophys. Res. Lett.*, *35*, L15102, doi:10.1029/2008GL034411.

Alexandrova, O., V. Carbone, P. Veltri, and L. Sorriso-Valvo (2008), Small-scale energy cascade of the solar wind turbulence, *Astrophys. J.*, *674*(2), 1153–1157.

Alexandrova, O., C. Lacombe, A. Mangeney, R. Grappin, and M. Maksimovic (2012), Solar wind turbulent spectrum at plasma kinetic scales, *Astrophys. J.*, *760*, 121, doi:10.1088/0004-637X/760/2/121.

Bagenal, F., and P. A. Delamere (2011), Flow of mass and energy in the magnetospheres of Jupiter and Saturn, *J. Geophys. Res.*, *116*, A05209, doi:10.1029/2010JA016294.

Bale, S. D., P. J. Kellogg, F. S. Mozer, T. S. Horbury, and H. Rème (2005), Measurement of the electric fluctuation spectrum of magnetohydrodynamic turbulence, *Phys. Rev. Lett.*, *94*, 215002.

Bourouaine, S., O. Alexandrova, E. Marsch, and M. Maksimovic (2012), On spectral breaks in the power spectra of magnetic fluctuations in fast solar wind between 0.3 and 0.9 AU, *Astrophys. J.*, *749*, 102.

Bruno, R., and V. Carbone (2005), The solar wind as a turbulence laboratory, *Living Rev. Sol. Phys.*, *2*(4), doi:10.12942/lrsp-2005-4.

Chané, E., J. Saur, and S. Poedts (2013), Modeling Jupiter's magnetosphere: Influence of the internal sources, *J. Geophys. Res. Space Physics*, *118*, 2157–2172, doi:10.1002/jgra.50258.

Chen, L., D. J. Wu, and J. Huang (2013), Kinetic Alfvén wave instability driven by field-aligned currents in a low plasma, *J. Geophys. Res. Space Physics*, *118*, 2951–2957, doi:10.1002/jgra.50332.

Cowley, S. W. H., and E. J. Bunce (2001), Origin of the main auroral oval in Jupiter's coupled magnetosphere-ionosphere system, *Planet. Space Sci.*, *49*, 1067–1088.

Dudok de Wit, T. (2004), Can high-order moments be meaningfully estimated from experimental turbulence measurements?, *Phys. Rev. E: Stat. Nonlinear Soft Matter Phys.*, *70*, 055302.

Frank, L. A., and W. R. Paterson (2002), Galileo observations of electron beams and thermal ions in Jupiter's magnetosphere and their relationship to the aurora, *J. Geophys. Res.*, *107*(A12), 1478, doi:10.1029/2001JA009150.

Frank, L. A., K. L. Ackerson, J. A. Lee, M. R. English, and G. L. Pickett (1992), The plasma instrumentation for the Galileo mission, *Space Sci. Rev.*, *60*, 283–307.

Galtier, S., S. V. Nazarenko, A. C. Newell, and A. Pouquet (2000), A weak turbulence theory for incompressible MHD, *J. Plasma Phys.*, *63*(5), 447–488.

Gary, S. P., and C. W. Smith (2009), Short-wavelength turbulence in the solar wind: Linear theory of whistler and kinetic Alfvén fluctuations, *J. Geophys. Res.*, *114*, A12105, doi:10.1029/2009JA014525.

Gary, S. P., S. Saito, and Y. Narita (2010), Whistler turbulence wave vector anisotropies: Particle-in-cell simulations, *Astrophys. J.*, *716*, 1332, doi:10.1088/0004-637X/716/2/1332.

Geiss, J., et al. (1992), Plasma composition in Jupiter's magnetosphere: Initial results from the solar wind ion composition spectrometer, *Science*, *257*, 1535–1539.

Glassmeier, K.-H. (1995), Ultralow frequency pulsations: Earth and Jupiter compared, *Adv. Space Res.*, *16*, 209–218.

Goldstein, M. L., D. A. Roberts, and C. A. Fitch (1994), Properties of the fluctuating magnetic helicity in the inertial and dissipation ranges of solar wind turbulence, *J. Geophys. Res.*, *99*(A6), 11,519–11,538, doi:10.1029/94JA00789.

Hanlon, P. G., M. K. Dougherty, N. Krupp, K. C. Hansen, F. J. Crary, D. T. Young, and G. Tóth (2004), Dual spacecraft observations of a compression event within the Jovian magnetosphere: Signatures of externally triggered supercorotation?, *J. Geophys. Res.*, *109*, A09S09, doi:10.1029/2003JA010116.

Hoshino, M., A. Nishida, T. Yamamoto, and S. Kokubun (1994), Turbulent magnetic field in the distant magnetotail: Bottom-up process of plasmoid formation?, *Geophys. Res. Lett.*, *21*, 2935–2938, doi:10.1029/94GL02094.

Howes, G. G., W. Dorland, S. C. Cowley, G. W. Hammett, E. Quataert, A. A. Schekochihin, and T. Tatsuno (2008), Kinetic simulations of magnetized turbulence in astrophysical plasmas, *Phys. Rev. Lett.*, *100*, 065004.

Huang, S. Y., F. Sahraoui, X. H. Deng, J. S. He, Z. G. Yuan, M. Zhou, Y. Pang, and H. S. Fu (2014), Kinetic turbulence in the terrestrial magnetosheath: Cluster observations, *Astrophys. J. Lett.*, *789*, L28, doi:10.1088/2041-8205/789/2/L28.

Joy, S. P., M. G. Kivelson, R. J. Walker, K. K. Khurana, C. T. Russell, and T. Ogino (2002), Probabilistic models of the Jovian magnetopause and bow shock locations, *J. Geophys. Res.*, *107*(A10), 1309, doi:10.1029/2001JA009146.

Kasahara, S., E. A. Kronberg, N. Krupp, T. Kimura, C. Tao, S. V. Badman, A. Retinò, and M. Fujimoto (2011), Magnetic reconnection in the Jovian tail: X line evolution and consequent plasma sheet structures, *J. Geophys. Res.*, *116*, A11219, doi:10.1029/2011JA016892.

Kasahara, S., E. A. Kronberg, T. Kimura, C. Tao, S. V. Badman, A. Masters, A. Retinò, N. Krupp, and M. Fujimoto (2013), Asymmetric distribution of reconnection jet fronts in the Jovian nightside magnetosphere, *J. Geophys. Res. Space Physics*, *118*, 375–384, doi:10.1029/2012JA018130.

Kivelson, M. G., K. K. Khurana, J. D. Means, C. T. Russell, and R. C. Snare (1992), The Galileo magnetic field investigation, *Space Sci. Rev.*, *60*(1–4), 357–383.
Kivelson, M. G., F. Bagenal, W. S. Kurth, F. M. Neubauer, C. Paranicas, and J. Saur (2004), Magnetospheric interactions with satellites, in *Jupiter: The Planet, Satellites, and Magnetosphere*, edited by F. Bagenal, T. Dowling, and W. McKinnon, pp. 513–536, Cambridge Univ. Press, Cambridge, U. K.
Kiyani, K. H., S. C. Chapman, F. Sahraoui, B. Hnat, O. Fauvarque, and Y. V. Khotyaintsev (2013), Enhanced magnetic compressibility and isotropic scale invariance at sub–ion larmor scales in solar wind turbulence, *Astrophys. J.*, *763*, doi:10.1088/0004-637X/763/1/10.
Klein, K. G., G. G. Howes, J. M. TenBarge, S. D. Bale, C. H. K. Chen, and C. S. Salem (2012), Using synthetic spacecraft data to interpret compressible fluctuations in solar wind turbulence, *Astrophys. J.*, *755*, 159, doi:10.1088/0004-637X/755/2/159.
Kronberg, E. A., J. Woch, N. Krupp, A. Lagg, K. K. Khurana, and K.-H. Glassmeier (2005), Mass release at Jupiter: Substorm-like processes in the Jovian magnetotail, *J. Geophys. Res.*, *110*, A03211, doi:10.1029/2004JA010777.
Krupp, N., A. Lagg, S. Livi, B. Wilken, J. Woch, E. C. Roelof, and D. J. Williams (2001), Global flows of energetic ions in Jupiter's equatorial plane: First-order approximation, *J. Geophys. Res.*, *106*(A11), 26,017–26,032, doi:10.1029/2000JA900138.
Leamon, R. J., C. W. Smith, N. F. Ness, W. H. Matthaeus, and H. K. Wong (1998), Observational constraints on the dynamics of the interplanetary magnetic field dissipation range, *J. Geophys. Res.*, *103*(A3), 4775–4787, doi:10.1029/97JA03394.
Mangeney, A., C. Lacombe, M. Maksimovic, A. A. Samsonov, N. Cornilleau-Wehrlin, C. C. Harvey, J.-M. Bosqued, and P. Travnicek (2006), Cluster observations in the magnetosheath: Part 1. Anisotropies of the wave vector distribution of the turbulence at electron scales, *Ann. Geophys.*, *24*(12), 3507–3521, doi:10.5194/angeo-24-3507-2006.
Matthaeus, W. H., and S. L. Lamkin (1986), Turbulent magnetic reconnection, *Phys. Fluids*, *29*, 2513.
Mauk, B. H., D. G. Mitchell, R. W. McEntire, C. P. Paranicas, E. C. Roelof, D. J. Williams, S. M. Krimigis, and A. Lagg (2004), Energetic ion characteristics and neutral gas interactions in Jupiter's magnetosphere, *J. Geophys. Res.*, *109*, A09S12, doi:10.1029/2003JA010270.
Miyoshi, T., and K. Kusano (2001), A global MHD simulation of the Jovian magnetosphere interacting with/without the interplanetary magnetic field, *J. Geophys. Res.*, *106*(A6), 10,723–10,742, doi:10.1029/2000JA900153.
Ogino, T., R. J. Walker, and M. G. Kivelson (1998), A global magnetohydrodynamic simulation of the Jovian magnetosphere, *J. Geophys. Res.*, *103*(A1), 225–235, doi:10.1029/97JA02247.
Perri, S., V. Carbone, and P. Veltri (2010), Where does fluid-like turbulence break down in the solar wind?, *Astrophys. J. Lett.*, *725*, L52–L55.
Podesta, J. J., and J. M. TenBarge (2012), Scale dependence of the variance anisotropy near the proton gyroradius scale: Additional evidence for kinetic Alfvén waves in the solar wind at 1 AU, *J. Geophys. Res.*, *117*, A10106, doi:10.1029/2012JA017724.
Radioti, A., N. Krupp, J. Woch, A. Lagg, K.-H. Glassmeier, and L. S. Waldrop (2005), Ion abundance ratios in the Jovian magnetosphere, *J. Geophys. Res.*, *110*, A07225, doi:10.1029/2004JA010775.
Russell, C. T., K. K. Khurana, M. G. Kivelson, and D. E. Huddleston (2000), Substorms at Jupiter: Galileo observations of transient reconnection in the near tail, *Adv. Space Res.*, *26*, 1499–1504.
Sahraoui, F. (2008), Diagnosis of magnetic structures and intermittency in space-plasma turbulence using the technique of surrogate data, *Phys. Rev. E*, *78*, 026402, doi:10.1103/PhysRevE.78.026402.
Sahraoui, F., G. Belmont, J. L. Pinçon, L. Rezeau, A. Balogh, P. Robert, and N. Cornilleau-Wehrlin (2004), Magnetic turbulent spectra in the magnetosheath: New insights, *Ann. Geophys.*, *22*, 2283–2288.
Sahraoui, F., G. Belmont, L. Rezeau, N. Cornilleau-Wehrlin, J. Pinçon, and A. Balogh (2006), Anisotropic turbulent spectra in the terrestrial magnetosheath as seen by the Cluster spacecraft, *Phys. Rev. Lett.*, *96*(7), 075002, doi:10.1103/PhysRevLett.96.075002.
Sahraoui, F., M. L. Goldstein, P. Robert, and Y. V. Khotyaintsev (2009), Evidence of a cascade and dissipation of solar wind turbulence at the electron gyroscale, *Phys. Rev. Lett.*, *102*, 231102.
Sahraoui, F., M. L. Goldstein, G. Belmont, P. Canu, and L. Rezeau (2010), Three-dimensional anisotropic *k* spectra of turbulence at sub–proton scales in the solar wind, *Phys. Rev. Lett.*, *105*(13), 131101, doi:10.1103/PhysRevLett.105.131101.
Sahraoui, F., G. Belmont, and M. L. Goldstein (2012), New insight into short-wavelength solar wind fluctuations from Vlasov theory, *Astrophys. J.*, *748*, 100.
Sahraoui, F., S. Y. Huang, G. Belmont, M. L. Goldstein, A. Retinò, P. Robert, and J. de Patoul (2013), Scaling of the electron dissipation range of solar wind turbulence, *Astrophys. J.*, *777*, 15, doi:10.1088/0004-637X/777/1/15.
Saur, J. (2004), Turbulent heating of Jupiter's middle magnetosphere, *Astrophys. J.*, *602*, L137–L140.
Saur, J., H. Politano, A. Pouquet, and W. Matthaeus (2002), Evidence for weak MHD turbulence in the middle magnetosphere of Jupiter, *Astron. Astrophys.*, *386*, 699.
Saur, J., A. Pouquet, and W. H. Matthaeus (2003), An acceleration mechanism for the generation of the main auroral oval on Jupiter, *Geophys. Res. Lett.*, *30*(5), 1260, doi:10.1029/2002GL015761.
Schekochihin, A. A., S. C. Cowley, W. Dorland, G. W. Hammett, G. G. Howes, E. Quataert, and T. Tatsuno (2009), Astrophysical gyrokinetics: Kinetic and fluid turbulent cascades in magnetized weakly collisional plasmas, *Astrophys. J. Suppl. Ser.*, *182*(1), 310–377, doi:10.1088/0067-0049/182/1/310.
Smith, C. W., K. Hamilton, and B. J. Vasquez (2006), Dependence of the dissipation range spectrum of interplanetary magnetic fluctuations on the rate of energy cascade, *Astrophys. J.*, *645*(1), 85–88, doi:10.1086/506151.
Stawicki, O., S. P. Gary, and H. Li (2001), Solar wind magnetic fluctuation spectra: Dispersion versus damping, *J. Geophys. Res.*, *106*(A5), 8273–8281, doi:10.1029/2000JA000446.
Tao, C., R. Kataoka, H. Fukunishi, Y. Takahashi, and T. Yokoyama (2005), Magnetic field variations in the Jovian magnetotail induced by solar wind dynamic pressure enhancements, *J. Geophys. Res.*, *110*, A11208, doi:10.1029/2004JA010959.
Thomas, N., F. Bagenal, T. W. Hill, and J. K. Wilson (2004), The Io neutral clouds and plasma torus, in *Jupiter: The Planet, Satellites, and Magnetosphere*, edited by F. Bagenal, T. Dowling, and W. McKinnon, pp. 561–591, Cambridge Univ. Press, Cambridge, U. K.
Uritsky, V. M., J. A. Slavin, G. V. Khazanov, E. F. Donovan, S. A. Boardsen, B. J. Anderson, and H. Korth (2011), Kinetic-scale magnetic turbulence and finite Larmor radius effects at Mercury, *J. Geophys. Res.*, *116*, A09236, doi:10.1029/2011JA016744.
von Papen, M., J. Saur, and O. Alexandrova (2014), Turbulent magnetic field fluctuations in Saturn's magnetosphere, *J. Geophys. Res. Space Physics*, *119*, 2797–2818, doi:10.1002/2013JA019542.
Vörös, Z., et al. (2004a), Magnetic turbulence in the plasma sheet, *J. Geophys. Res.*, *109*, A11215, doi:10.1029/2004JA010404.
Vörös, Z., W. Baumjohann, R. Nakamura, A. Runov, M. Volwerk, T. L. Zhang, and A. Balogh (2004b), Wavelet analysis of magnetic turbulence in the Earth's plasma sheet, *Phys. Plasmas*, *11*, 1333–1338, doi:10.1063/1.1667499.
Weygand, J. M., et al. (2005), Plasma sheet turbulence observed by Cluster II, *J. Geophys. Res.*, *110*, A01205, doi:10.1029/2004JA010581.
Woch, J., N. Krupp, and A. Lagg (2002), Particle bursts in the Jovian magnetosphere: Evidence for a near-Jupiter neutral line, *Geophys. Res. Lett.*, *29*(7), 1138, doi:10.1029/2001GL014080.
Yordanova, E., A. Vaivads, M. André, S. C. Buchert, and Z. Vörös (2008), Magnetosheath plasma turbulence and its spatiotemporal evolution as observed by the cluster spacecraft, *Phys. Rev. Lett.*, *100*(20), 205003.
Zimbardo, G., A. Greco, L. Sorriso-Valvo, S. Perri, Z. Vörös, G. Aburjania, K. Chargazia, and O. Alexandrova (2010), Magnetic turbulence in the geospace environment, *Space Sci. Rev.*, *156*, 89–134.